This article has been accepted for publication in IEEE Transactions on Automation Science and Engineering. This is the author's version which has not been fully edited and content may change prior to final publication. Citation information: DOI 10.1109/TASE.2025.3585644

A Coarse-to-fine Robotic Fabric Alignment System Integrating Visual Servoing and Admittance Control

Jiaming Qi*, Liang Lu*, Lei Yang, Yan Ding, Pai Zheng, *Senior Member, IEEE*, David Navarro-Alarcon, *Senior Member, IEEE*, Jia Pan†, *Senior Member, IEEE* and Peng Zhou†, *Member, IEEE*

***Abstract*—Fabric alignment is essential to key production processes such as cutting, sewing, and fusing in garment manufacturing. Traditionally, this task has relied heavily on the dexterity and expertise of skilled human workers. Although automated systems have been introduced, they often lack the flexibility required for complex alignment tasks. In this paper, we present a novel robotic fabric alignment framework that fully automates the process with high precision and adaptability. First, we propose a coarse-to-fine alignment strategy, where an initial imprecise target position is roughly computed based on a basic perception module and eye-to-hand calibration. This is followed by a sliding mode control (SMC)-based visual servoing approach (in an eye-in-hand configuration) to ensure a close-up view of feedback features for the fine alignment process. Additionally, we consider system disturbances estimated by a fuzzy logic system (FLS) and combine it with the controller to further enhance the system's robustness. Finally, we developed an advanced end-effector equipped with force/torque (F/T) sensors and air-powered needle grippers for gentle fabric manipulation using admittance control. We validate our framework through a series of experiments that demonstrate its effectiveness in fabric alignment tasks.**

***Note to Practitioners*—Fabric alignment in garment production is a labor-intensive task that heavily relies on skilled human workers. Existing automated fabric alignment machines are typically limited to specific fabric shapes, patterns, and materials. Furthermore, transitioning between different fabric types requires extensive testing and adjustments, resulting in a lack of adaptability and flexibility. In this work, we propose a robotic fabric alignment system based on a coarse-to-fine alignment strategy. The initial target pose is roughly estimated using a basic perception module and eye-to-hand calibration, followed by fine adjustments through a visual servoing controller in an eye-in-hand configuration. Additionally, to ensure gentle handling, the contact force between the end-effector and the platform surface is optimized using admittance control. The proposed system offers practitioners a comprehensive solution for automating fabric alignment with high precision, while maintaining flexibility and adaptability across various fabric types and initial environmental conditions.**

***Index Terms*—Automation; Fabric manipulation; Visual servoing; Admittance control.**

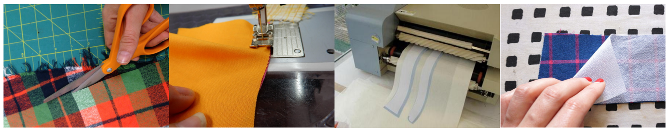

Fig. 1. Fabric alignment is a fundamental task essential to various garment manufacturing processes, including (from left to right) fabric cutting, sewing, fusing, and pattern matching.

I. INTRODUCTION

Robotic automation has significantly advanced various industrial processes, leading to improvements in efficiency and precision across industries and manufacturing sectors [1], [2]. However, garment production faces distinct difficulties that make it different from other automated fields [3]. In contrast to industries like car assembly or electronics, where robots mainly deal with hard parts, garment manufacturing requires handling soft, flexible materials [4]–[7] such as fabric, rope.

Fabrics are deformable objects that easily change shape when subjected to external forces. However, fabric manipulation is integral across all stages of the garment production process. Among all the production processes, fabric alignment is a critical operation in garment manufacturing, serving as the foundation for key processes such as cutting, sewing, and fusing (see Fig. 1). The precision of fabric alignment directly affects the quality and efficiency of these processes, making it essential for achieving consistent, high-quality production. Traditionally, fabric alignment has been performed manually, relying on the dexterity and experience of skilled workers to ensure accuracy. While automated systems have been introduced to streamline production, they are often rigid and struggle to adapt to the inherent variability of fabrics, such as changes in texture, elasticity, and shape. These limitations pose significant challenges, particularly in an industry that requires flexibility to accommodate frequent shifts in fashion trends and production demands. As a result, there is a growing need for more advanced automation solutions that can handle the complexity of fabric alignment with greater precision and adaptability.

To develop a robotic system that meets the requirements, we conducted a detailed analysis of expert human workers performing fabric alignment and identified key practices that ensure high precision. Drawing on these insights, we integrated two air-powered needle grippers and designed a specialized robotic end-effector capable of securely grasping both ends of

---

This work is supported by the National Natural Science Foundation of China (NSFC) under Grant No. 62403211, in part by the Innovation and Technology Commission of the HKSAR Government through InnoHK Initiative, General Research Fund (GRF) under Grant No. 17200924 and No. 17201025, and in part by RGC-NSFC under Grant N_HKU70524. Corresponding author: *Jia Pan and Peng Zhou*

*Authors with equal contribution. † Corresponding author.

J. Qi is with the College of Mechanical and Electrical Engineering, Northeast Forestry University, Heilongjiang, China.

L. Lu, L. Yang and J. Pan are with the Department of Computer Science, The University of Hong Kong, Pok Fu Lam, Hong Kong.

Y. Ding is with the Shanghai Artificial Intelligence Laboratory.

P. Zheng and D. Navarro-Alarcon are with The Hong Kong Polytechnic University, Kowloon, Hong Kong.

P. Zhou is with the School of Advanced Engineering, The Great Bay University, Dongguan, China.

the fabric. This design minimizes deformation during fabric handling, thereby improving both alignment accuracy and operational efficiency. We also proposed a coarse-to-fine alignment strategy, beginning with an initial rough computation of the target alignment position using a basic perception module and eye-to-hand calibration. This is followed by a sliding mode control (SMC)-based visual servoing approach (in an eye-in-hand configuration) to provide close-up feedback for the fine alignment process, mimicking the detailed visual feedback techniques used by skilled workers during fabric alignment.

To further enhance the system's robustness, we incorporated a fuzzy logic system (FLS)-based approach to estimate system disturbances, which is integrated into the controller design. Additionally, admittance control was implemented to enable robust yet delicate grasping and placement of fabrics in various configurations, ensuring stable and gentle handling of fabrics with diverse properties. We validated our framework through a series of experiments that demonstrated its effectiveness in fabric alignment tasks.

The contributions of this paper are summarized as follows:

- We leverage a coarse-to-fine alignment strategy to propose a novel robotic fabric alignment system with high precision and adaptability.
- We propose a new sliding mode control (SMC)-based visual servoing controller that utilizes a fuzzy logic system (FLS) to estimate disturbances, and thus, provides adaptiveness and robustness.
- We develop an advanced end-effector equipped with force/torque (F/T) sensors and air-powered needle grippers for gentle fabric manipulation, and considering stable robot grasping through admittance control.

The rest of this article is organized as follows. In Section II, we carefully discuss the advantages and limitations of current mainstream approaches for fabric manipulation. The problem formulation is discussed in Section III. In Section IV, we provide a brief overview of admittance control in this paper. Fabric identification approach is presented in Section V. Details of the visual servoing-based fabric alignment control design and stability analysis are presented in Section VI. Experimental results are shown in Section VII. Section VIII presents concluding remarks and future work.

II. RELATED WORK

This section reviews the literature on deformable object manipulation (DOM) [8], focusing specifically on fabric manipulation and object alignment. It highlights the progression from traditional methods to more advanced, adaptive strategies.

A. Traditional Fabric Manipulation Techniques

In garment manufacturing, the majority of processes are still performed manually, with only a small portion of specific tasks being fully automated. Traditional approaches to fabric manipulation automation often rely on mechanical solutions, which are typically task-specific and lack the flexibility required to handle the variability and complexity of fabrics. For example, [9] introduces a versatile gripper capable of executing a wide range of grasps, simplifying tasks such as picking up folded garments or folding fabric in mid-air. Similarly, [10] designs an innovative robotic gripper inspired by human grasping strategies for handling fabric materials. Building on this, [11] proposes automation technologies for common manufacturing processes in garment factories. Despite these advancements, traditional systems rely heavily on rigid-contact approaches for fabric manipulation. This reliance limits their adaptability and precision, particularly when dealing with fabrics of varying characteristics or operating in unstructured environments.

B. Visual Servoing and Admittance Control

Advancements in computer vision have made visual servoing a significant breakthrough in fabric manipulation [12]. In [13], system feedback is used to train a pseudo-kinematic model, which is then applied to folding and sorting tasks. The authors further extend their research to various manipulation tasks, demonstrating improved system stability and precision compared to purely mechanical methods [14]. Similarly, [15] introduces a model-based closed-loop control framework to enable human-robot collaboration for cooperative fabric manipulation. [16] presents a collaborative object transportation approach, enhancing the accuracy of deformation detection through data-driven depth estimation. Additionally, a grasping framework is proposed in [17] to support diverse grasping strategies for hybrid grippers. However, these methods often require multiple iterative manipulations to determine optimal robot actions, making them less suitable for industrial applications where speed and efficiency are crucial.

Admittance control, on the other hand, enables robot-environment interaction by adjusting the robot's movements based on force feedback [18]. For example, [19] proposes a physical human-robot interaction approach using a robotic exoskeleton to address unknown dynamic characteristics. Subsequently, [20] develops an admittance-based controller for coordinated operations within constrained task spaces, preventing collisions with the environment. Combining admittance control with visual servoing offers a robust solution for managing the unpredictable dynamics of fabric manipulation, making it particularly advantageous in tasks requiring adaptability and precision. However, existing fabric alignment techniques struggle with real-world complexities like fabric uncertainties, environmental factors, and robot interactions, due to a lack of integration between visual servoing, force control, and compensation mechanisms, resulting in reduced accuracy and reliability.

In contrast, we propose an innovative control framework that seamlessly integrates visual servoing with admittance control and a Fuzzy Logic System-based compensation mechanism. By holistically addressing force interactions and variable environmental conditions, the framework achieves superior alignment performance, as validated by experimental results. Furthermore, it shows great potential for high-precision tasks such as pick-and-place operations, making it a versatile solution for robotic applications in precision manufacturing.

III. SYSTEM OVERVIEW

Notation: A vector and a matrix are denoted by lowercase and uppercase bold letters, respectively, e.g., $\mathbf{v}$ and $\mathbf{M}$. ${}^{\mathcal{F}_x}\mathbf{p}$ represents a point $\mathbf{p}$ within the frame $\mathcal{F}_x$. By default, all points

This article has been accepted for publication in IEEE Transactions on Automation Science and Engineering. This is the author's version which has not been fully edited and content may change prior to final publication. Citation information: DOI 10.1109/TASE.2025.3585644

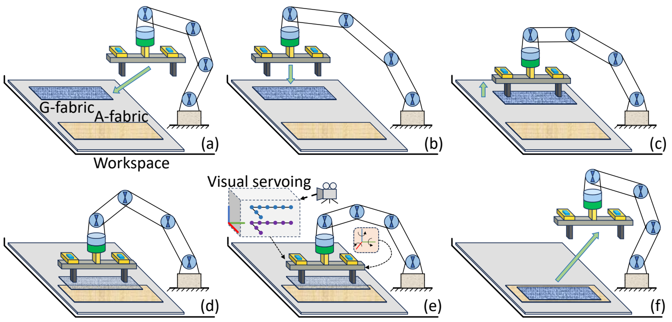

Fig. 2. The graphical schematic of the fabric alignment. The green arrow indicates the direction of the robot's movement. (a) Initially, the G-fabric (blue fabric) and A-fabric (yellow fabric) are randomly positioned in the workspace. (b) The robot moves above the G-fabric. (c) The robot grasps the G-fabric and lifts it. (d) The robot then positions the G-fabric above the A-fabric while maintaining a specified distance for initial alignment. (e) Visual servoing is activated to facilitate the alignment process. (f) Finally, the G-fabric and A-fabric are aligned according to the specified requirements.

are defined in the world frame $\mathcal{F}_w$. ${}^{\mathcal{F}a}\mathbf{T}_{\mathcal{F}_b} \in SE(3)$ denotes the transformation from frame $\mathcal{F}_a$ to frame $\mathcal{F}_b$.

Fig. 2 shows the schematic illustration of the designed fabric alignment framework. The proposed framework is designed to address challenges in textile, garment manufacturing, and other fabric processing industries. The core idea is to achieve the fabric alignment task under specific requirements through visual feedback, it enables robotic systems to handle complex fabric shapes and adapt to external force variations, thereby improving production efficiency and quality. As depicted in Fig. 3, this work introduces a coarse-to-fine robotic fabric alignment strategy, which consists of two stages: coarse alignment and fine alignment. In the coarse alignment stage, the system captures the pose of the fabric to be grasped (G-fabric) and the fabric to be aligned (A-fabric). In the fine alignment stage, a carefully designed visual servoing algorithm is employed to align the two fabrics based on visual fabric feature feedback. Additionally, admittance control is applied to ensure stable contact between the fixture and the workspace, enabling reliable fabric grasping and placement.

The following assumptions are made: i) The robot moves the fabric slowly, avoiding shaking, which is common with soft objects during manipulations. ii) The fabric lies within the robot's reachable range. iii) The fabric can be separated from the workspace using specific methods, such as color thresholds. iv) Fabric alignment conducted on the same plane can be transformed into maintaining a separation distance between fabrics. This transformation is referred to as the Manipulation Equivalence of fabric alignment.

IV. ADMITTANCE CONTROL

As the fabric is placed on a rigid workspace, using a hard-contact reaching approach (bypassing the pose directly) may result in collisions between the fixture and the workspace [21]. To address this issue, admittance control is employed to ensure safety between the robot and the workspace while maintaining stable grasping and placement of the fabric. Admittance control operates with pose control as the inner loop and force control as the outer loop, adjusting the robot's motion based on contact forces [22]. A second-order transformation model is used to compute the correction pose $\mathbf{x}_c$, which is fed into the inner loop to achieve stable pose control. The correction pose is derived as follows:

$$\ddot{\mathbf{x}}_c = \mathbf{A}_m^{-1}(\mathbf{F}_e - \mathbf{A}_b\dot{\mathbf{x}}_e - \mathbf{A}_k\mathbf{x}_e) \tag{1}$$

where $\ddot{\mathbf{x}}_c$ is the desired acceleration. $\mathbf{A}_m$, $\mathbf{A}_b$, and $\mathbf{A}_k$ are symmetric positive-definite matrices representing inertia, damping, and stiffness, respectively. $\mathbf{F}_e$ is the difference between the feedback force $\mathbf{F}$ and the desired force $\mathbf{F}_d$. $\mathbf{x}_e$ represents the difference between the feedback pose $\mathbf{x}$ and the desired pose $\mathbf{x}_d$.

The Runge-Kutta 4th-order method (RK4) [23] is used to integrate Equation (1) and compute $\mathbf{x}_c$. The actual pose is then calculated as $\mathbf{x}_{\text{actual}} = \mathbf{x}_c + \mathbf{x}_d$, where $\mathbf{x}_d$ represents the grasping or placement pose, detailed in Sec. V. Fig. 4 provides the block diagram of the admittance control. When the robot comes into contact with the workspace (during grasping or placement), the fixture must securely press against the workspace while maintaining a consistent down-pressure along the z-axis of the force/torque (F/T) sensor to ensure stable contact. The wrench formula is used to transform $\mathbf{F}_d = [0, 0, f_z, 0, 0, 0]^\intercal$ in the F/T frame into the world frame when using Equation (1).

V. FABRIC IDENTIFICATION

A. Fabric Classification

In this work, two fabrics with the same configuration but different areas are used. For simplicity, the fabric area serves as the metric to distinguish between the two fabrics. Fig. 5 illustrates the segmented G-fabric and A-fabric.

B. Feature Detection

By applying *OpenCV/findContours* to the segmented fabrics and performing de-projection from the depth image using known camera intrinsic and extrinsic parameters, the Cartesian contour points in $\mathcal{F}_w$ are obtained as follows:

$$\mathbf{t} = [\mathbf{t}_1, \ldots, \mathbf{t}_{n_c}]^\intercal, \qquad \mathbf{d} = [\mathbf{d}_1, \ldots, \mathbf{d}_{n_c}]^\intercal \tag{2}$$

Here, $\mathbf{t}$ and $\mathbf{d}$ represent the contour points for the G-fabric and A-fabric, respectively, and n_c is the number of contour points. Both $\mathbf{t}$ and $\mathbf{d}$ are ordered, and their respective centers are denoted as $\bar{\mathbf{t}}$ and $\bar{\mathbf{d}}$.

The fabric is asymmetrical, with one side being concave and the other side approximately straight. We define the points along the quasi-straight line as the side points, denoted as $\mathbf{t}_s$ for the G-fabric and $\mathbf{d}_s$ for the A-fabric.

C. Frame Definition

For simplicity, the establishment of the G-fabric frame $\mathcal{F}_t$ and the A-fabric frame $\mathcal{F}_d$ is introduced. Due to the unevenness of the fabric, the A-fabric and G-fabric are not perfectly co-planar. Therefore, an optimal surface covering the fabric must be determined for subsequent grasping and placement. $\mathcal{F}_t$ is used as an example to provide a generalized representation.

The general surface equation is formulated as $h_x x + h_y y + h_z z + h_d = 0$, where $\Omega = [h_x, h_y, h_z, h_d]^\intercal$ is the hyperparameter. The construction takes the form $\mathbf{f}_i = [\mathbf{t}_i^\intercal, 1]^\intercal$, where

This article has been accepted for publication in IEEE Transactions on Automation Science and Engineering. This is the author's version which has not been fully edited and content may change prior to final publication. Citation information: DOI 10.1109/TASE.2025.3585644

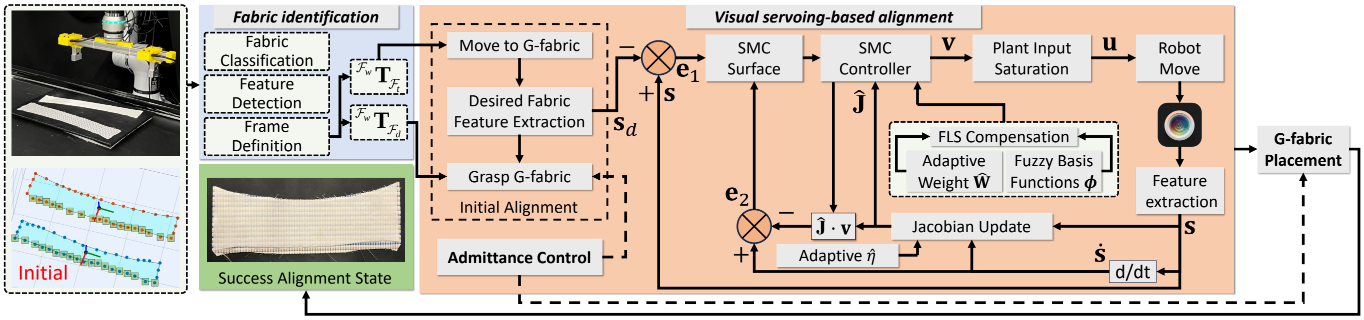

Fig. 3. The structure of the visual servoing-based fabric alignment framework. The blue box represents the fabric identification module, which provides pre-grasping and pre-placement poses. The pink box represents the coarse alignment stage and the fine alignment stage.

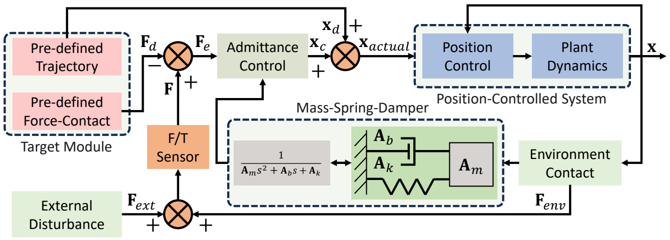

Fig. 4. The block diagram of the admittance control.

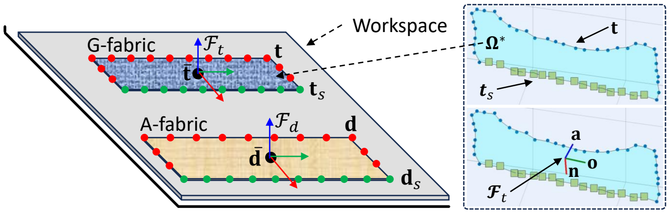

Fig. 5. The visualization of the fabric identification, including fabric classification, feature detection, and frame definition.

$i \in [1, n_c]$. Using the distance between $\mathbf{t}$ and the surface defined by the optimal hyperparameter Ω^*, the following cost function is constructed:

$$\begin{aligned} \Omega^* &= \underset{\Omega\in\mathbb{R}^4}{\arg\min} \sum_{i=1}^{n_c} \left(\Omega^\intercal \mathbf{f}_i / \sqrt{h_x^2+h_y^2+h_z^2}\right)^2 \\ \text{s.t.} \quad & |\Omega^\intercal \mathbf{f}_i| / \sqrt{h_x^2+h_y^2+h_z^2} \le \delta_1, \quad i \in [1, n_c] \end{aligned} \tag{3}$$

where δ_1 is the distance threshold controlling the fitting accuracy. Equation (3) minimizes the sum of distances between $\mathbf{t}$ and the surface while ensuring that each point-to-surface distance remains below the threshold. The nonlinear solver [24] is applied to Equation (3) to compute Ω^*.

The normal vector of Ω^* is then used as the z-axis of $\mathcal{F}_t$, defined as $\mathbf{a} = [h_x, h_y, h_z]^\intercal / |[h_x, h_y, h_z]|$. To ensure $\mathbf{a}$ forms an acute angle with the positive z-axis, $\text{dot}(\mathbf{a}, [0, 0, 1])$ is calculated. If the result is negative, $\mathbf{a}$ is reversed. Fig. 5 illustrates the determination of the optimal surface Ω^*.

The direction vector along $\mathbf{t}_s$ is used as the y-axis of $\mathcal{F}_t$. Principal Component Analysis (PCA) [25] is applied to $\mathbf{t}_s$ to obtain the principal component, which is normalized and used as the y-axis: $\mathbf{o} = \text{PCA}(\mathbf{t}_s)_{\text{main}}$. The x-axis of $\mathcal{F}_t$ is calculated using the right-hand rule as $\mathbf{n} = (\mathbf{o} \times \mathbf{a}) / |\mathbf{o} \times \mathbf{a}|$.

Setting $\bar{\mathbf{t}}$ as the origin $\mathbf{p}$ ensures uniqueness. The transformation matrix from $\mathcal{F}_w$ to $\mathcal{F}_t$ is defined as:

$${}^{\mathcal{F}_w}\mathbf{T}_{\mathcal{F}_t} = \begin{bmatrix} \mathbf{n} & \mathbf{o} & \mathbf{a} & \mathbf{p} \\ 0 & 0 & 0 & 1 \end{bmatrix} \tag{4}$$

Finally, repeating the above process for the A-fabric yields ${}^{\mathcal{F}_w}\mathbf{T}_{\mathcal{F}_d}$. Fig. 5 shows the fabric identification results.

VI. VISUAL SERVOING-BASED FABRIC ALIGNMENT

We define the studied fabric alignment as a classic visual servoing task [26], focusing on extracting task-specific visual features and tracking their changes. First, the desired fabric feature is introduced, followed by the presentation of the robot-fabric kinematic relationship. Next, a servoing controller is constructed to achieve fabric alignment, and finally, the system's stability is proven, including approximation and control. The end-effector's pose is defined as $\mathbf{r} \in \mathbb{R}^6$, and the velocity command $\mathbf{u} = \dot{\mathbf{r}}$ serves as the control input to be designed.

A. Desired Fabric Feature

As shown in Fig. 2b, the robot moves above the G-fabric using ${}^{\mathcal{F}_w}\mathbf{T}_{\mathcal{F}_t}$ as defined in Equation (4). At this point, the fixture maintains a fixed distance δ_2 above the G-fabric. Since only the G-fabric is visible in the camera view, the 2D boundary pixels belonging to the G-fabric can be easily extracted using simple image processing algorithms. Subsequently, the 3D boundary points are computed using the camera's intrinsic parameters and are considered the desired fabric feature $\mathbf{s}_d$. This approach establishes a direct one-to-one correspondence between 2D pixels and 3D points, enhancing robustness against measurement noise [5].

B. Initial Alignment

After extracting $\mathbf{s}_d$, the fixture descends to grasp the G-fabric. However, due to measurement bias, ${}^{\mathcal{F}_w}\mathbf{T}_{\mathcal{F}_t}$ may not accurately represent the G-fabric's pose. This deviation can cause the fixture to either remain too far from the workspace or apply excessive downward pressure, potentially causing mechanical damage. To address this issue, admittance control is applied to ensure stable grasping while simultaneously avoiding excessive contact between the fixture and the workspace. The robot securely grasps the G-fabric, as shown in Fig. 2c. It then moves above the A-fabric using ${}^{\mathcal{F}_w}\mathbf{T}_{\mathcal{F}_d}$, maintaining the same distance δ_2 as before.

C. Feedback Fabric Feature

After performing the initial alignment, the system transitions into the state shown in Fig. 2d. At this stage, only the two symmetrically positioned eye-in-hand depth cameras are used to observe the workspace during the visual servoing process. First, the 2D boundary pixels from the images captured by the two depth cameras are collected. These pixels belong to the fabric (without distinguishing between the two fabrics at this point). Then, as before, the 3D boundary points Ω are calculated. Next, it is necessary to distinguish Ω into the G-fabric and A-fabric. An intuitive approach would be to use the depth values for classification. However, this can result in inaccuracies because the depth-value range of Ω is typically small. To address this issue, K-means clustering (KMS) [27] is applied for classification, resulting in the G-fabric boundary points Ω_{top} and the A-fabric boundary points Ω_{down}. Finally, Ω_{down} is used as the feedback feature $\mathbf{s}$.

Remark 1. The main contribution of this paper lies in the proposed vision-based servoing framework for fabric alignment. The selection of fabric features is not the focus of this study, therefore simple boundary points are used as visual features to validate the effectiveness of the proposed framework. For complex fabric configurations, it can design specialized visual features, such as spatial angles or triangular areas.

D. Model Establishment

When the system is in the state shown in Fig. 2d, slight movements of the end-effector cause subtle changes in the fabric feature. The kinematic relationship between $\mathbf{s}$ and $\mathbf{r}$ is defined as the sensorimotor model [28] in the alignment servoing task, expressed as $\mathbf{s} = \mathbf{f}(\mathbf{r})$. Traditionally, an approximate difference equation is directly obtained. However, in this paper, to ensure system stability, several disturbances are considered during the modeling process, followed by compensation design.

Discretization disturbance: Using the Taylor expansion combined with the backward difference formula, the first-order kinematic model is expressed as:

$$\dot{\mathbf{s}} = \frac{\partial \mathbf{f}}{\partial \mathbf{r}}\dot{\mathbf{r}} + \mathbf{d}_s(\mathbf{s}, \mathbf{r}) = \mathbf{J}\mathbf{u} + \mathbf{d}_s(\mathbf{s}, \mathbf{r}) \tag{5}$$

where $\mathbf{J}$ is the kinematic Jacobian matrix (KJM) that transforms robot motions into feature changes, and $\mathbf{d}_s(\mathbf{s}, \mathbf{r})$ is the Taylor expansion remainder. The matrix $\mathbf{J}$ can be regarded as the local motion model of the fabric under quasi-static manipulation by the robot. In practice, it is challenging to compute $\mathbf{J}$ analytically (i.e., $\partial \mathbf{f}/\partial \mathbf{r}$) because the physical properties of the fabric are generally *unknown*. Instead of identifying the full mechanical model, this paper proposes an algorithm to compute local approximations of $\mathbf{J}$ in real time.

Approximation disturbance: As the KJM is estimated online, it is divided into two components: $\mathbf{J} = \hat{\mathbf{J}} + \tilde{\mathbf{J}}$, where $\hat{\mathbf{J}}$ is the numerical estimation of $\mathbf{J}$, and $\tilde{\mathbf{J}}$ represents the approximation error. Combining this with Equation (5) gives:

$$\dot{\mathbf{s}} = \hat{\mathbf{J}}\mathbf{u} + \mathbf{d}_J(\tilde{\mathbf{J}}, \mathbf{u}) + \mathbf{d}_s(\mathbf{s}, \mathbf{r}), \quad \mathbf{d}_J(\tilde{\mathbf{J}}, \mathbf{u}) = \tilde{\mathbf{J}}\mathbf{u} \tag{6}$$

where $\mathbf{d}_J(\tilde{\mathbf{J}}, \mathbf{u})$ represents the uncertainty in system modeling caused by the KJM estimation errors.

Saturation Disturbance: In real-world applications, to achieve rapid tracking, the system often outputs a large control command, which can lead to input saturation nonlinearity. Ignoring the effects of saturation can weaken system performance and even damage actuators [29]. The common solving solution is the hard saturation technique [30], however, it may lead to discontinuities and abrupt changes, potentially leading to system oscillations [31]. For the above issues, we propose the following anti-saturation control law to approximate the saturation nonlinearity [32]:

$$\begin{aligned} u(v) &= u_b \cdot \mathrm{erf}\Big(v \cdot \frac{\sqrt{\pi}}{2u_b}\Big), \quad \mathrm{erf}(x) = \frac{2}{\sqrt{\pi}} \int_0^x e^{-t^2}\, \mathrm{d}t \\ u_b &= \Big(\bar{u}_b + \frac{1}{2}\underline{u}_b\Big) + \Big(\bar{u}_b - \frac{1}{2}\underline{u}_b\Big)\,\mathrm{sgn}(v) \end{aligned} \tag{7}$$

where v is the designed control input, while $u(v)$ is the actual control input after the saturation effect. $\mathrm{sgn}(\cdot)$ is the sign function, and $\mathrm{erf}(\cdot)$ is the Gaussian error function [32]. The advantages of choosing Equation (7) are: i) It provides a smooth transition for the input signal as it approaches the saturation limits, rather than being abruptly truncated, allowing for continuous variation and avoiding abrupt changes and oscillations; ii) It can effectively simulate nonlinear behavior, allowing the control system to maintain a certain level of responsiveness even when approaching saturation. iii) By maintaining continuous response, it helps to minimize nonlinear effects, contributing to system stability and dynamic performance. iv) The upper and lower saturation limits can be flexibly adjusted by $\bar{u}_b$ and $\underline{u}_b$, i.e., when $\bar{u}_b = \underline{u}_b$, the saturation model becomes symmetric. In this paper, we apply saturation limits to the end-effector's pose, i.e., $\mathbf{u} = \{u_i\}, \mathbf{v} = \{v_i\}, i \in [1, 6]$. The saturation error is defined as $\Delta(\mathbf{v}) = \mathbf{u} - \mathbf{v}$, it yields

$$\mathbf{u} = \mathbf{v} + \Delta(\mathbf{v}) \tag{8}$$

Total disturbance: Substituting Equation (8) into Equation (6) gives:

$$\dot{\mathbf{s}} = \hat{\mathbf{J}}\mathbf{v} + \underbrace{\mathbf{d}_u(\hat{\mathbf{J}}, \Delta\mathbf{v}) + \mathbf{d}_J(\tilde{\mathbf{J}}, \mathbf{u}) + \mathbf{d}_s(\mathbf{s}, \mathbf{r})}_{\mathbf{d}(\mathbf{s}, \mathbf{r})} \tag{9}$$

where $\mathbf{d}_u(\hat{\mathbf{J}}, \Delta(\mathbf{v})) = \hat{\mathbf{J}}\Delta(\mathbf{v})$ represents the saturation disturbance, and $\mathbf{d}(\mathbf{s}, \mathbf{r})$ is the total disturbance.

Finally, the system in Equation (9) simplifies to:

$$\dot{\mathbf{s}} = \hat{\mathbf{J}}\mathbf{v} + \mathbf{d}(\mathbf{s}, \mathbf{r}) \tag{10}$$

where $\mathbf{v}$ is the control input to be designed later.

Remark 2. Since we consider regular fabrics, it is reasonable to assume that slight $\dot{\mathbf{r}}$ will produce slight $\dot{\mathbf{s}}$. As the Cartesian points obtained from the camera model are used as visual features, a one-to-one mapping relationship $\mathbf{s} = \mathbf{f}(\mathbf{r})$ is assumed to hold locally.

E. Fuzzy Approximation

To enhance system stability, the fuzzy logic system (FLS) [33] is introduced to model the nonlinear disturbance $\mathbf{d}(\mathbf{s}, \mathbf{r})$ and compensate for it within the system. This results in:

$$\mathbf{d}(\mathbf{s}, \mathbf{r}) = \mathbf{W}^{\intercal}\boldsymbol{\phi} + \varepsilon \tag{11}$$

This article has been accepted for publication in IEEE Transactions on Automation Science and Engineering. This is the author's version which has not been fully edited and content may change prior to final publication. Citation information: DOI 10.1109/TASE.2025.3585644

where $\mathbf{W}$ is the ideal constant weight matrix, and $\boldsymbol{\phi}$ is the pre-defined fuzzy basis vector [33]. The matrix $\mathbf{W}$ is unknown and requires online estimation. Let $\hat{\mathbf{W}}$ denote the numerical estimate of $\mathbf{W}$, and $\tilde{\mathbf{W}} = \mathbf{W} - \hat{\mathbf{W}}$ represent the estimation error. FLS is used to estimate the total disturbance and compensate for it within the controller.

Lemma 1. *[33] For any $x \in \mathbb{R}$ and any $\kappa > 0$, it is certain that: $0 \le |x| - x\tanh(x/\kappa) \le 0.2785\kappa$.*

Lemma 2. *[33] For any continuous vector $\mathbf{f}(\mathbf{x})$ defined on the compact set Ω, and for any constant vector $\varepsilon > 0$, the FLS satisfies the following property:*

$$\sup_{\mathbf{x}\in\Omega} \|\mathbf{f}(\mathbf{x}) - \mathbf{W}^\intercal\boldsymbol{\phi}(\mathbf{x})\| \le \|\varepsilon\| \tag{12}$$

Assumptions 1. There exists an ideal weight matrix $\mathbf{W}$ such that $|\varepsilon|^2 \le \eta$, where $\eta > 0$ is a constant for all $\mathbf{x} \in \Omega$.

F. Controller Design

Sliding mode control (SMC) is introduced to achieve closed-loop alignment. Two tracking errors are defined as:

$$\mathbf{e}_1 = \mathbf{s} - \mathbf{s}_d, \qquad \mathbf{e}_2 = \dot{\mathbf{s}} - \hat{\mathbf{J}}\mathbf{v} \tag{13}$$

where $\mathbf{e}_1$ represents the alignment error and $\mathbf{e}_2$ represents the model estimation error. Here, $\mathbf{s}_d$ is the desired fabric feature defined in Sec. VI-A. Notably, $\mathbf{s}_d$ can be time-varying, representing an improvement over methods that assume it to be constant [34]. Through Equation (13), SMC integrates model estimation and controller design while providing a unified stability analysis.

By computing the time derivative of Equation (13), we obtain:

$$\dot{\mathbf{e}}_1 = \dot{\mathbf{s}} - \dot{\mathbf{s}}_d, \qquad \dot{\mathbf{e}}_2 = \ddot{\mathbf{s}} - \dot{\hat{\mathbf{J}}}\mathbf{v} - \hat{\mathbf{J}}\dot{\mathbf{v}} \tag{14}$$

The sliding mode surfaces are constructed as:

$$\boldsymbol{\sigma}_1 = \mathbf{K}_1\mathbf{e}_1 + \dot{\mathbf{e}}_1, \qquad \boldsymbol{\sigma}_2 = \mathbf{K}_2\mathbf{e}_2 + \dot{\mathbf{e}}_2 \tag{15}$$

where $\mathbf{K}_1$ and $\mathbf{K}_2$ are symmetric positive-definite constant matrices that regulate the convergence speed of $\boldsymbol{\sigma}_1$ and $\boldsymbol{\sigma}_2$. Ensuring the convergence of $\boldsymbol{\sigma}_1$ guarantees the convergence of $\mathbf{e}_1$, meaning $\mathbf{s}$ approaches $\mathbf{s}_d$. This completes the fabric alignment task. Theoretically, SMC-based control systems offer superior robustness compared to conventional feedback control systems [5]. Using Equation (11) and Equation (14), the time derivative of $\boldsymbol{\sigma}_1$ is given by:

$$\dot{\boldsymbol{\sigma}}_1 = \mathbf{K}_1(\hat{\mathbf{J}}\mathbf{v} + \mathbf{W}^\intercal\boldsymbol{\phi} + \varepsilon - \dot{\mathbf{s}}_d) + \ddot{\mathbf{e}}_1 \tag{16}$$

The velocity controller is designed as:

$$\begin{aligned} \mathbf{v} &= \hat{\mathbf{J}}^{+}\mathbf{K}_1^{-1}(-\boldsymbol{\sigma}_1 + \mathbf{K}_1\dot{\mathbf{s}}_d - \ddot{\mathbf{e}}_1 - \mathbf{K}_1\hat{\mathbf{W}}^\intercal\boldsymbol{\phi}) \\ \dot{\hat{\mathbf{W}}} &= \Gamma(\boldsymbol{\phi}\boldsymbol{\sigma}_1^\intercal\mathbf{K}_1 - \beta\hat{\mathbf{W}}) \end{aligned} \tag{17}$$

where $\hat{\mathbf{J}}^{+}$ is the pseudo-inverse of $\hat{\mathbf{J}}$, $\Gamma > 0$ is the coefficient matrix, and β is a small positive constant. Since the design avoids power terms and the sign function, $\mathbf{v}$ remains continuous, preventing chattering. To ensure system convergence, the quadratic function is defined as $V_1(\boldsymbol{\sigma}_1) = \frac{1}{2}\boldsymbol{\sigma}_1^\intercal\boldsymbol{\sigma}_1$. By computing the time derivative of V_1 and using Equation (16) and Equation (17), we have:

$$\dot{V}_1(\boldsymbol{\sigma}_1) = -\boldsymbol{\sigma}_1^\intercal\boldsymbol{\sigma}_1 + \boldsymbol{\sigma}_1^\intercal\mathbf{K}_1\varepsilon + \boldsymbol{\sigma}_1^\intercal\mathbf{K}_1\tilde{\mathbf{W}}^\intercal\boldsymbol{\phi} \tag{18}$$

Referencing Assumption 1 and applying Young's inequality, the following relation is obtained:

$$\boldsymbol{\sigma}_1^\intercal\mathbf{K}_1\varepsilon \le \frac{1}{4}\lambda_{\mathbf{K}_1}^2\|\boldsymbol{\sigma}_1\|^2 + \eta \tag{19}$$

where $\lambda_{\mathbf{K}_1}$ denotes the maximum eigenvalue of $\mathbf{K}_1$. Substituting Equation (19) into Equation (18), we have:

$$\dot{V}_1(\boldsymbol{\sigma}_1) \le -(1 - \frac{1}{4}\lambda_{\mathbf{K}_1}^2)\|\boldsymbol{\sigma}_1\|^2 + \boldsymbol{\sigma}_1^\intercal\mathbf{K}_1\tilde{\mathbf{W}}^\intercal\boldsymbol{\phi} + \eta \tag{20}$$

The KJM is adaptively computed as:

$$\begin{aligned} \dot{\hat{\mathbf{J}}} &= (\ddot{\mathbf{s}} - \hat{\mathbf{J}}\dot{\mathbf{v}} - \mathbf{K}_2^{-1}\boldsymbol{\varpi})\mathbf{v}^{+} \\ \boldsymbol{\varpi} &= -\boldsymbol{\sigma}_2 - \ddot{\mathbf{e}}_2 - \boldsymbol{\sigma}_2^{\intercal +}\tanh(\frac{1}{\gamma_1})\hat{\eta}, \quad \dot{\hat{\eta}} = \tanh(\frac{1}{\gamma_1}) - \gamma_2\hat{\eta} \end{aligned} \tag{21}$$

where γ_1 and γ_2 are positive constants. The term $\ddot{\mathbf{s}} - \hat{\mathbf{J}}\dot{\mathbf{v}}$ reflects the updates of $\mathbf{s}$ and $\mathbf{v}$ with respect to $\hat{\mathbf{J}}$. The term $\boldsymbol{\varpi}$ compensates for system modeling errors, thereby improving stability. The parameter $\hat{\eta}$ compensates for the FLS approximation error, and the estimation error is given by $\tilde{\eta} = \eta - \hat{\eta}$.

The adaptive rule $\dot{\hat{\eta}}$ employs the δ-modification algorithm [35] to address parameter drift caused by estimation errors. It is important to note that this rule does not guarantee identification of the true value of $\mathbf{J}$. Instead, its objective is to compute a numerical solution for $\mathbf{J}$ that continuously satisfies the system model Equation (10).

Similarly, the quadratic function for $\boldsymbol{\sigma}_2$ is defined as: $V_2(\boldsymbol{\sigma}_2) = \frac{1}{2}\boldsymbol{\sigma}_2^\intercal\boldsymbol{\sigma}_2$. Using Equation (21), the time-derivative of V_2 yields:

$$\dot{V}_2(\boldsymbol{\sigma}_2) = -\boldsymbol{\sigma}_2^\intercal\boldsymbol{\sigma}_2 - \tanh(1/\gamma_1)\hat{\eta} \tag{22}$$

G. Stability Analysis

Proposition 1. *Consider the closed-loop system Equation (10) under Assumption 1, with the velocity controller Equation (17), the model estimator Equation (21), and the adaptive rule $\dot{\hat{\eta}}$. Given the desired fabric feature $\mathbf{s}_d$, there exists an appropriate set of control parameters that ensure: (i) all signals remain uniformly ultimately bounded (UUB), and (ii) the alignment error $\mathbf{e}_1$ asymptotically converges to a compact set around zero.*

proof: Consider the following quadratic function:

$$V = V_1(\boldsymbol{\sigma}_1) + \frac{\mathrm{tr}(\tilde{\mathbf{W}}^\intercal\Gamma^{-1}\tilde{\mathbf{W}})}{2} + V_2(\boldsymbol{\sigma}_2) + \frac{\tilde{\eta}^2}{2} \tag{23}$$

Computing the time-derivative of Equation (23), we obtain:

$$\dot{V} = \boldsymbol{\sigma}_1^\intercal\dot{\boldsymbol{\sigma}}_1 - \mathrm{tr}(\tilde{\mathbf{W}}^\intercal\Gamma^{-1}\dot{\hat{\mathbf{W}}}) + \boldsymbol{\sigma}_2^\intercal\dot{\boldsymbol{\sigma}}_2 - \tilde{\eta}\dot{\hat{\eta}} \tag{24}$$

Using Young's inequality, the following relations are derived:

$$\begin{aligned} \gamma_2\tilde{\eta}\hat{\eta} &\le -\frac{\gamma_2}{2}\tilde{\eta}^2 + \frac{\gamma_2}{2}\eta^2 \\ \mathrm{tr}(\tilde{\mathbf{W}}^\intercal\beta\hat{\mathbf{W}}) &\le -\frac{\beta}{2}\left\|\tilde{\mathbf{W}}\right\|^2 + \frac{\beta}{2}\|\mathbf{W}\|^2 \end{aligned} \tag{25}$$

Taking into account Equation (18), Equation (22), Equation (25), the adaptive rules for $\dot{\hat{\eta}}$ and $\dot{\hat{\mathbf{W}}}$, and Lemma 1, we have:

$$\dot{V} \leq -aV + b \tag{26}$$

where $a = \min(2 - \lambda^2_{\mathbf{K}_1}/2, 2, \beta, \gamma_2)$, and the residual term is $b = \beta\|\mathbf{W}\|^2/2 + \gamma_2\eta^2/2 + 0.2785\gamma_1\eta > 0$. By selecting an appropriate value for $\mathbf{K}_1$ to ensure $a > 0$, the states $\boldsymbol{\sigma}_1$, $\boldsymbol{\sigma}_2$, $\tilde{\mathbf{W}}$, and $\tilde{\eta}$ exhibit asymptotic convergence and remain UUB. This result guarantees that $\mathbf{e}_1$ will eventually converge to a compact set near zero. Furthermore, it demonstrates that the estimation error $\tilde{\mathbf{J}}$ is bounded.

■

The SMC employed is a type of overdetermined controller, meaning $\mathbf{e}_1$ can only converge to a local range determined by the feasibility of $\mathbf{s}_d$. In visual servoing, the local minimization problem based on the Jacobian formulation is inevitable [5]. Algorithm 1 outlines the proposed fabric alignment framework. The parameter $\delta_3 > 0$ regulates the alignment accuracy.

Algorithm 1 Fabric alignment process

```
Require:
Fabric identification in Sec. V ← ${}^{\mathcal{F}_w}\mathbf{T}_{\mathcal{F}_t}$ and ${}^{\mathcal{F}_w}\mathbf{T}_{\mathcal{F}_d}$
The robot moves to ${}^{\mathcal{F}_w}\mathbf{T}_{\mathcal{F}_t}$
Calculate the desired fabric feature $\mathbf{s}_d$
Grasp the G-fabric + Admittance control: $\mathbf{x}_d \leftarrow {}^{\mathcal{F}_w}\mathbf{T}_{\mathcal{F}_t}$
The robot moves the G-fabric to ${}^{\mathcal{F}_w}\mathbf{T}_{\mathcal{F}_d}$
The robot conducts tiny movements to initialize $\hat{\mathbf{J}}(0)$
Start the visual servoing
while $\|\mathbf{e}_1\| \geq \delta_3$ do
    Record the current robot pose $\mathbf{r}$ and velocity $\mathbf{u}$
    Record the current fabric feature $\mathbf{s}$
    Calculate the error signals $\mathbf{e}_1$ and $\mathbf{e}_2$ ← Equation (13)
    Calculate the surfaces $\boldsymbol{\sigma}_1$ and $\boldsymbol{\sigma}_2$ ← Equation (15)
    Update the FLS weight $\dot{\hat{\mathbf{W}}}$ ← Equation (17)
    Update the velocity command $\mathbf{v}$ ← Equation (17)
    Update the KJM $\dot{\hat{\mathbf{J}}}$ ← Equation (21)
    Update the plant input $\mathbf{u}$ ← Equation (7)
    The robot moves using the updated $\mathbf{u}$
end while
Place the G-fabric + Admittance control: $\mathbf{x}_d \leftarrow {}^{\mathcal{F}_w}\mathbf{T}_{\mathcal{F}_d}$
Fabric alignment is completed
```

VII. EXPERIMENTAL RESULTS

To validate the proposed fabric alignment system, we design a flowchart, as shown in Fig. 6, to execute the task and collect statistical data for the experimental results. In this process, Initial Alignment, Visual Servoing, and Final Phase represent the main components, while Admittance Control ensures stable grasping and placement of the fabric. Initially, coarse alignment is achieved using the estimated ${}^{\mathcal{F}_w}\mathbf{T}_{\mathcal{F}_t}$ and ${}^{\mathcal{F}_w}\mathbf{T}_{\mathcal{F}_d}$. Then, a visual servoing-based control strategy is implemented for fine alignment. Finally, performance metrics are calculated to verify whether the alignment task is complete.

A. *Platform Setup*

Fig. 7 illustrates the experimental setup for validating the fabric alignment tasks. A RealSense RGB-D calibrated D455 camera is used to observe the initial alignment from a top-down perspective, following an eye-to-hand configuration. The HansRobot (Model: E05) is employed as the robotic platform, as shown in Fig. 7a. A KWR75B 6-DOF F/T sensor is used to detect the contact force between the robot and the environment, enabling admittance control. A zero-offset calibration was conducted to ensure accurate measurements, as shown in Fig. 7b. The setup combines a 3030 aluminum profile with 3D-printed fabric fixtures installed at the end of the F/T sensor. Two pneumatic needle-type suction cups (Model: WJ-T20*45) are used as fabric grippers. These suction cups are attached to the aluminum profile via 3D-printed connectors and are horizontally positioned at both ends of the profile, as shown in Fig. 7e. A high-pressure air hose (6 bar) from the laboratory's built-in system is connected to a program-controlled solenoid valve, which is managed by the computer, as shown in Fig. 7c and Fig. 7d. Two RealSense RGB-D D405 cameras are horizontally mounted at both ends of the aluminum profile using 3D-printed connectors, following an eye-in-hand configuration. Both D405 cameras provide visual feedback without requiring extrinsic calibration. To ensure a comprehensive evaluation, two scenarios are considered: flat placement and tilted placement. Each scenario includes two fabric positioning configurations. Fig. 7f - Fig. 7i depict the four cases.

To meet the assumptions outlined in Sec. III, the saturation limit for 3-DOF translation is set to 0.03 m/s, while for 3-DOF rotation, it is set to 10°/s. The proposed algorithm is implemented in Ubuntu 20.04 using the ROS1/Python API interface. Image processing, alignment control, and admittance control operate within a servo-control loop running at 28 Hz. The used fabric is custom-made for industrial production and has predefined dimensions, allowing boundary points on both sides to be extracted as feedback feature points.

B. *Validation of Admittance Control*

In this section, we evaluate the admittance control introduced in Sec. IV. Fig. 8a shows the validation setup. A custom 3D-printed handle is made to allow for free dragging of the end-effector. For simplicity, the admittance control is simplified to consider translation control without rotation here. $\mathbf{F}_d = [0, 0, 0]^\intercal$ in the F/T frame, and the measured $\mathbf{F}$ should be converted into the world frame.

Three desired trajectories $\mathbf{x}_d$ are adopted, namely spatial helix, spatial ellipse, and spatial straight, see Fig. 8b. This is done to verify the adaptive nature of admittance control in regulating external human contact force. The robot is firstly commanded to reach the initial position $\mathbf{x}_d(0)$. Then, the robot starts tracking $\mathbf{x}_d$ while we randomly contact the F/T sensor. Normally, the robot will move in the direction along the contact force, achieving *"escaping"* the contact of the hand. When external contact disappears, the robot continues tracking $\mathbf{x}_d$. We conduct four experiments for each $\mathbf{x}_d$, considering different dominance scenarios: $\mathbf{A}_m$ dominance (Setting 1), $\mathbf{A}_b$ dominance (Setting 2), $\mathbf{A}_k$ dominance (Setting 3), and a combined dominance (Setting 4). Table I gives four settings.

This article has been accepted for publication in IEEE Transactions on Automation Science and Engineering. This is the author's version which has not been fully edited and content may change prior to final publication. Citation information: DOI 10.1109/TASE.2025.3585644

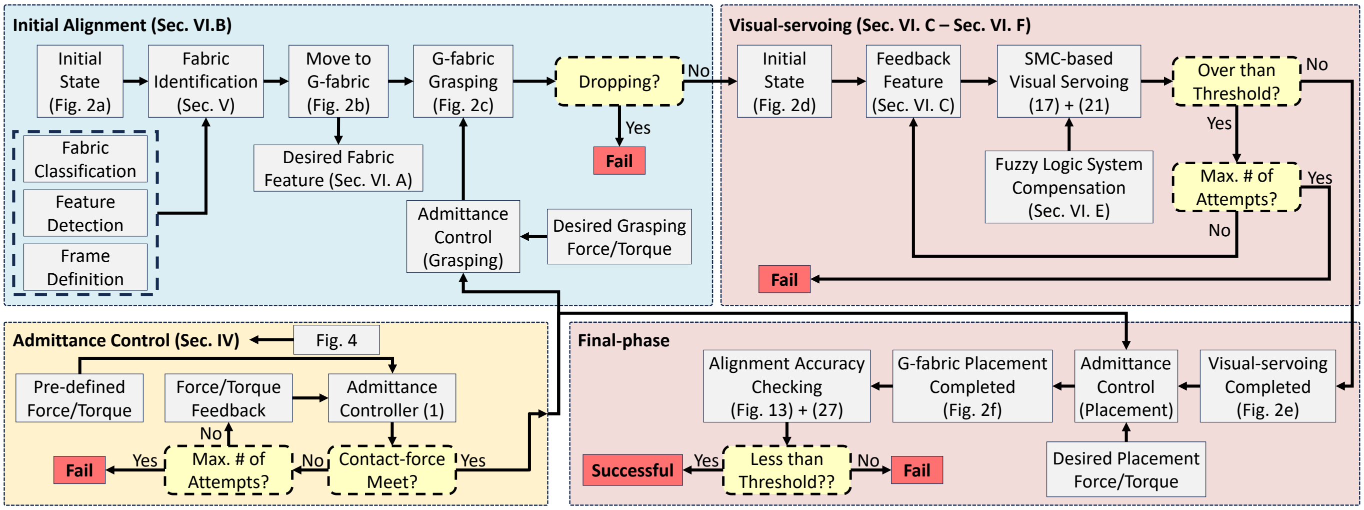

Fig. 6. Flowchart of the fabric alignment framework. It includes: i) Initial Alignment: the robot grasps the G-fabric and moves above the A-fabric to achieve a preliminary alignment. ii) Visual Servoing: the robot achieves the "final step" fine alignment through visual feedback. iii) Admittance Control: responsible for compliant manipulation during the grasping and placement of the fabric. iv) Final Phase: determining whether the fabric alignment task is completed.

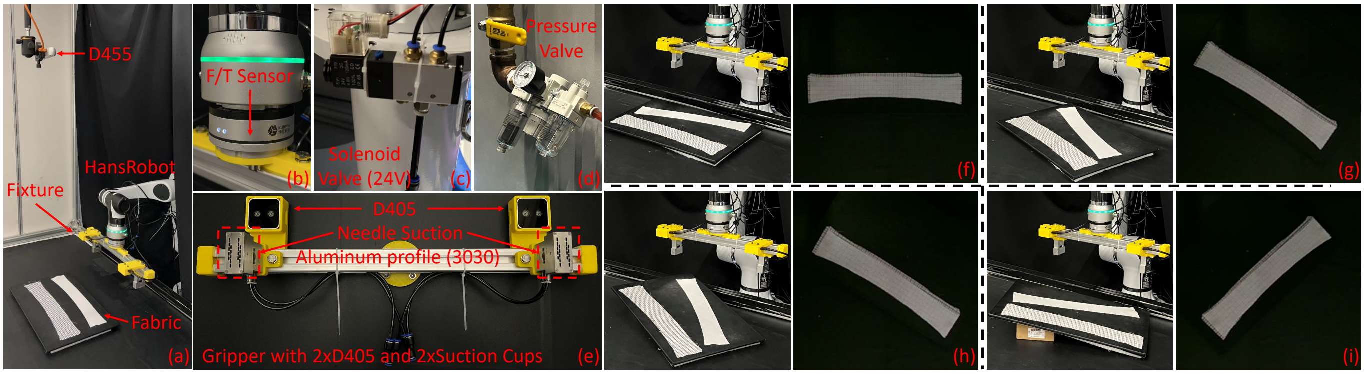

Fig. 7. (a)-(e): experimental setup; (f) - (i): the alignment of fabrics in four placement configurations, where the left subplots show the initial states and the right subplots show the final aligned states. (f) and (g): Fabrics are placed on the ground, initially oriented in opposite directions. (h) and (i): Fabrics are placed on a slope, also oriented in opposite directions.

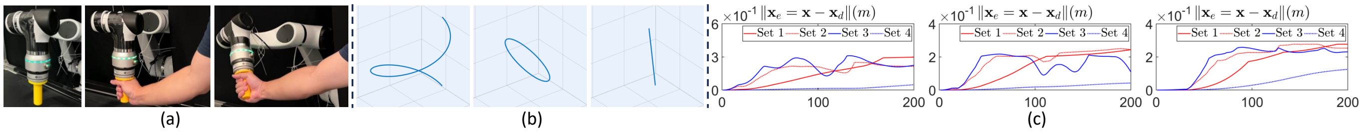

Fig. 8. The platform description of the admittance validation and results presentation. (a) The yellow 3D-printed handle is designed to assist human in applying external forces to the end-effector, and two different grasping postures for instance. (b) Three adopted configurations of $\mathbf{x}_d$, i.e., spatial helix, spatial ellipse, spatial straight, respectively. (c) The tracking profiles of $\|\mathbf{x}_e\|$ of three types of $\mathbf{x}_d$. The display sequence is the same as in (b). Each subplot includes four components of Setting 1 - Setting 4. The abscissa is the step size.

Fig. 8c presents the profiles of admittance control under three $\mathbf{x}_d$ tracking scenarios. Each subplot includes a comparison between four sets of hyper-parameters and $\mathbf{x}_d$. The results illustrate that when $\mathbf{A}_m$ dominates, the system initially exhibits good compensation with a smooth form. However, the system shows a noticeable lag over time. This indicates that $\mathbf{A}_m$ has a feed-forward compensation effect on the system. When the frequency of external contact forces is high (corresponding to $\mathbf{F}_e$), the performance of feed-forward compensation can be adjusted by tuning $\mathbf{A}_m$. $\mathbf{A}_b$ has a similar effect to $\mathbf{A}_m$, but excessive $\mathbf{A}_b$ can cause significant fluctuations in $\mathbf{x}_c$, thus affecting the effectiveness of compliant compensation. Additionally, appropriately adjusting $\mathbf{A}_b$ can mitigate the lag effects caused by $\mathbf{A}_m$ to some extent. When $\mathbf{A}_k$ dominates, the system exhibits the strongest response to $\mathbf{F}_e$ and can respond at the fastest speed. This is because $\mathbf{A}_m$ and $\mathbf{A}_b$ act in the feed-forward compensation stage, while $\mathbf{A}_k$ directly affects the negative feedback loop. However, when $\mathbf{A}_k$ is too large, the fluctuations in $\mathbf{x}_c$ become even more intense. This is because $\mathbf{A}_k$ is directly added to $\mathbf{x}_e$, resulting in a non-smooth curve. Moreover, in extreme cases (such as sudden large-magnitude impacts of external forces), this can cause significant displacement and affect the tracking performance of the system. Through the above experimental analysis, it concludes that $\mathbf{A}_m$ controls the system's inertia, which determines the rate of response to input forces.

This article has been accepted for publication in IEEE Transactions on Automation Science and Engineering. This is the author's version which has not been fully edited and content may change prior to final publication. Citation information: DOI 10.1109/TASE.2025.3585644

TABLE I
PARAMETERS SETTING ($\mathbf{A}_m, \mathbf{A}_b, \mathbf{A}_k$) OF THE ADMITTANCE CONTROL VALIDATION. THE TILTED NUMBERS IN EACH GROUP REPRESENT THE PARAMETER VALUES THAT REQUIRE SPECIFIC VALIDATION. SETTING 4 IS OUR FINAL-ADOPTED PARAMETERS.

	Parameter setting 1	Parameter setting 2	Parameter setting 3	Final setting 4
Helix	(*4.5926*, 0.5792, 0.1325)	(0.4829, *3.5939*, 0.9689)	(0.2654, 0.4898, *6.6581*)	(2.5789, 4.6986, 3.1498)
Ellipse	(*3.5815*, 1.5892, 1.2689)	(1.3651, *5.5938*, 1.8759)	(1.5687, 1.9568, *4.3453*)	(3.5937, 5.6894, 4.3459)
Straight	(*2.3251*, 0.1065, 0.1059)	(0.1065, *3.3285*, 0.1025)	(0.1035, 0.1084, *3.5789*)	(1.6895, 3.3258, 2.2696)

$\mathbf{A}_b$ controls the damping effect in the system, affecting its buffering capacity and stability. $\mathbf{A}_k$ represents the system's resistance to displacement. Throughout the following sections, $\mathbf{A}_m, \mathbf{A}_b, \mathbf{A}_k = (2.5289, 4.5978, 3.2519)$, respectively.

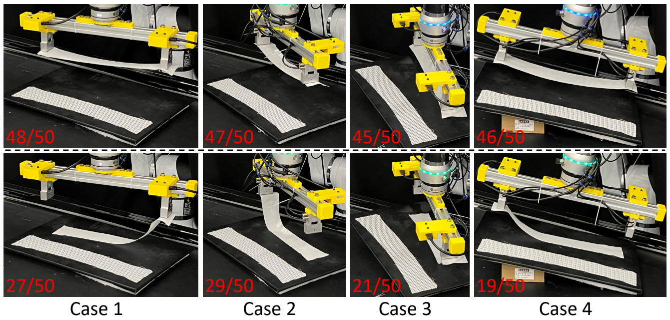

Fig. 9. The fabric grasping with (first row) and without (second row) admittance control in four placement configurations shown in Fig. 7. The bottom left corner of the image indicates the success rate of the grasping.

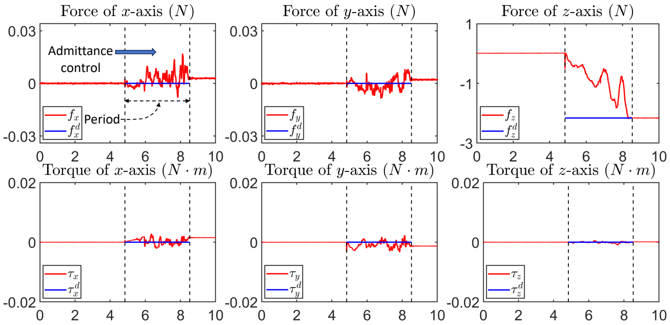

Fig. 10. F/T profiles for Case 1, with time (s) on the abscissa.

C. Validation of Admittance Control Related to Manipulation

In this section, admittance control is applied during the grasping and placing of the G-fabric. For simplicity, we focus on fabric grasping. Four cases shown in Fig. 7 (Cases 1–4) are used. $\mathbf{F}_d = [0, 0, -2.16, 0, 0, 0]$ in the F/T frame, and $-2.16N$ represents the desired contact force along the z-axis of the F/T frame. The effects of using and not using admittance control are verified from the following aspects.

Firstly, the success rate is calculated by repeating each grasping scenario fifty times, and the grasping pose is determined using Equation (4). Fig. 9 presents the grasping results. The results show that admittance control significantly improves the success rate (highlighted in red). Although it is possible to manually adjust the end-effector's pose to regulate the downward force, such adjustments are open-loop in nature and can easily result in mechanical actuator failures or damage to the workspace. Fig. 10 illustrates the F/T profiles for Case 1. The red line represents the F/T feedback, while the blue line indicates the desired signal. Since admittance control activates when the fixture contacts the workspace, the blue line is presented intermittently. The admittance control starts at 4.84 s and ends at 8.53 s. Fig. 10 clearly demonstrates that admittance control effectively maintains stable contact forces and torques. For the 3-DOF force, static contact is achieved along the xy-axes, while constant pressure is quickly established along the z-axis. For the 3-DOF torque, although the curves deviate visibly from the desired values, this is due to the small units on the vertical axis. Despite these deviations, the zero rotational energy of the 3-DOF torque is effectively maintained.

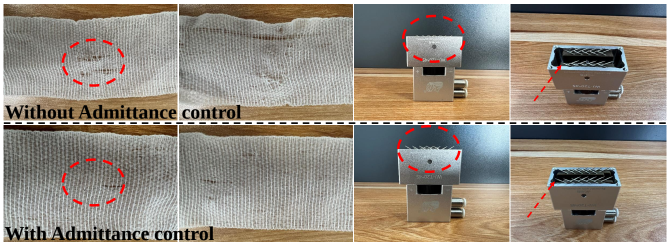

Fig. 11. Display of the fabric surface state and the needle-type suction cup state with and without admittance control. The first row represents the state without admittance control, while the second row represents the state with admittance control.

Fig. 11 shows the state of the fabric and suction cup after 50 repeated grasps. The results indicate that, as a needle-type suction cup is used, without the effect of admittance control, there is a high likelihood of surface damage to the fabric and bending deformation of the needle due to excessive rigid contact. In contrast, with admittance control, the fabric maintains a good surface condition (with no obvious signs of tearing) even after multiple grasping. The right two columns show that when admittance control is not used, repeated grasping leads to a reduction in the maximum extension distance of the needle. This is due to excessive collisions between the suction cup and the table, resulting in mechanical damage. The above results show that admittance control not only ensures the integrity of the fabric but also prevents mechanical failures caused by excessive contact between the suction cup and the surface.

Additionally, due to the inaccuracies in camera calibration, the measured ${}^{\mathcal{F}_w}\mathbf{T}_{\mathcal{F}_t}$ and ${}^{\mathcal{F}_w}\mathbf{T}_{\mathcal{F}_d}$ may be incorrect. Without admittance control, this deviation could lead to excessive or insufficient contact between the suction cup and the surface. In contrast, employing admittance control can partially compensate for the effects of calibration errors, allowing for stable contact between the suction cup and the surface, and enabling safe fabric manipulation.

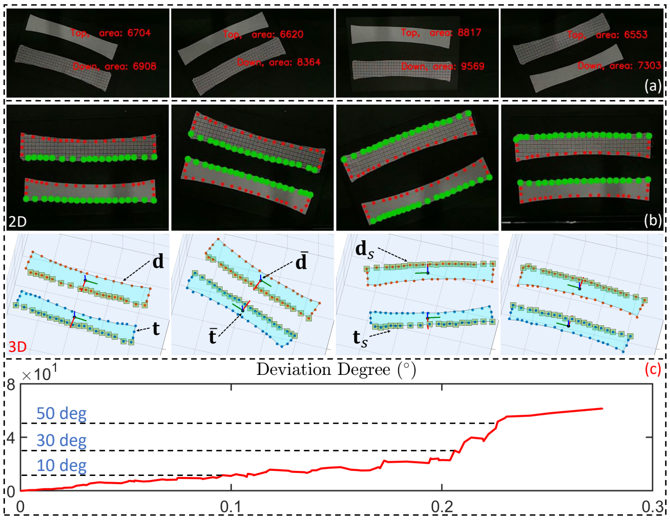

Fig. 12. Validations of fabric identification. (a) Fabric classification based on fabric area. (b) Feature detection and frame definition. (c) The profile between the fabric surface flatness and the z-axis calculated by Equation (3).

D. Validation of Fabric Identification

Fig. 12a shows the fabric classification results of two differently sized fabrics in various positions. The striped fabric represents the A-fabric, while the white textured fabric represents the G-fabric. The results demonstrate that distinguishing fabric types based on the area metric is effective across different positions.

Fig. 12b illustrates the detection of contour points ($\mathbf{t}$ and $\mathbf{d}$), center points ($\bar{\mathbf{t}}$ and $\bar{\mathbf{d}}$), and side points ($\mathbf{t}_s$ and $\mathbf{d}_s$). The RGB image from the D455 camera is converted into a binary image using mask processing. Farthest Point Sampling (FPS) [36] is applied to extract a fixed set of contour pixels. Subsequently, the 3D contour points are computed by mapping the corresponding 2D pixels using the intrinsic and extrinsic camera parameters. The results show that the contour points are evenly arranged, effectively representing the boundary information, and the detection of side points is precise.

Fig. 12b also depicts the fabric frames ($\mathcal{F}_t$ and $\mathcal{F}_d$). The light blue region represents the optimal co-planar surface of the fabric contour points ($\mathbf{t}$ or $\mathbf{d}$), determined using Equation (3), which is used to establish the z-axis of the fabric frame. Notably, the z-axis of the fabric frame forms an acute angle with the z-axis of $\mathcal{F}_w$. The y-axis of the fabric frame is constrained to be horizontally oriented to the right along the fabric surface. The results confirm that Equation (4) accurately establishes the directional fabric frame, significantly aiding subsequent grasping and placement tasks.

To further validate the effectiveness of Equation (3) in calculating the z-axis, we present the relationship between fabric flatness and deviation angle. The fabric flatness is obtained by calculating the standard deviation of the z-axis for $\mathbf{t}$ and $\mathbf{d}$, while the deviation angle is the difference between the calculated z-axis and the theoretical z-axis (0,0,1). The fabric is placed on a flat table with varying degrees of wrinkling. Fig. 12c indicates that when the flatness is less than 0.2, the deviation angle changes approximately linearly. However, when it exceeds 0.2, the error curve rises sharply. Additionally, since the deviation angle in practical applications is typically less than 10 degrees, it is evident from the figure that it is approximately below 0.1. Therefore, Equation (3) effectively ensures the accuracy of the z-axis calculation. The potential reason is that the nonlinear constraint in Equation (3) aims to limit the distance from each point to the fitted plane, thereby mitigating the impact of wrinkles to some extent. Applying a clustering method to the wrinkled regions can help reduce the influence of wrinkle-induced point sampling on $\mathbf{t}$ and $\mathbf{d}$.

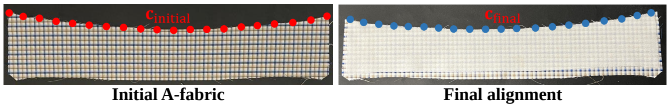

Fig. 13. Visualization of the alignment error calculation.

E. Alignment Metric Definition

Three metrics are used to evaluate alignment performance: success rate, running time, and alignment error. Inspired by [37], we use the following technique to assess alignment accuracy. At the start, we record the contour points on the alignment edge (i.e., arc edge) of the A-fabric (fixed sampling of 20 points). These points are inverse-mapped to Cartesian space using the camera model and recorded as $\mathbf{c}_{\text{initial}}$. Subsequently, after alignment is completed, a skilled worker with extensive fabric processing experience manually traces the contour points of the G-fabric, recorded as $\mathbf{c}_{\text{final}}$. The alignment error (mm) is then calculated using the Mean Squared Error (MSE):

$$\text{Error} = \frac{1}{20}\sum_{i=1}^{20} \|\mathbf{c}_{\text{initial}}\{i\} - \mathbf{c}_{\text{final}}\{i\}\| \tag{27}$$

Fig. 13 illustrates the alignment error calculation process. The red points represent $\mathbf{c}_{\text{initial}}$, sampled at the initial moment, while the blue points represent $\mathbf{c}_{\text{final}}$, manually annotated by the experienced worker after alignment is completed. Due to the soft texture of the fabric and the needle-like gripper used, repeated grasping and placing actions cause deformation along the fabric edges. Even when grasping and placing at the same location, the fabric undergoes slight deformations, resulting in fluctuations in alignment error calculations. Successful cases refer to stable grasping and placing with alignment errors below $5mm$. Meanwhile, running time and alignment error are calculated only for successful cases.

F. Same Shape-size Fabric Alignment

The experimental scenarios utilize the four placement configurations depicted in Fig. 7. Due to space constraints, only the scenarios shown in Fig. 7g and Fig. 7i are presented. Three baseline methods (a), (b), (c) and the proposed method (d) are are employed for a comprehensive performance comparison in each scenario. All approaches are implemented based on SMC. Admittance control is not applied in approaches (a) and (b), resulting in a hard-contact method for grasping and placement.

This article has been accepted for publication in IEEE Transactions on Automation Science and Engineering. This is the author's version which has not been fully edited and content may change prior to final publication. Citation information: DOI 10.1109/TASE.2025.3585644

TABLE II
COMPARISON RESULTS OF THREE INDICES UNDER FOUR PLACEMENT CONFIGURATIONS SHOWN IN FIG. 7 AND FOUR COMPARATIVE APPROACHES.

	Case 1			Case 2			Case 3			Case 4		
	Success rate	Running time (s)	Alignment Error (mm)	Success rate	Running time (s)	Alignment Error (mm)	Success rate	Running time (s)	Alignment Error (mm)	Success rate	Running time (s)	Alignment Error (mm)
(a)	11/20	32.1 ± 0.69	4.79 ± 1.37	11/20	44.1 ± 0.67	4.89 ± 1.24	9 /20	25.3 ± 0.77	4.96 ± 1.69	10/20	36.2 ± 0.87	5.12 ± 1.77
(b)	12/20	33.7 ± 0.75	3.14 ± 0.57	13/20	46.1 ± 0.81	3.25 ± 0.53	11/20	28.9 ± 0.61	3.96 ± 0.61	10/20	38.6 ± 0.81	4.02 ± 0.59
(c)	15/20	35.1 ± 0.87	4.86 ± 1.38	16/20	48.9 ± 0.73	4.98 ± 1.32	14/20	30.1 ± 0.82	4.75 ± 1.67	16/20	40.6 ± 0.89	4.91 ± 1.75
(d)	19/20	37.6 ± 0.68	3.13 ± 0.49	18/20	50.8 ± 0.77	2.97 ± 0.55	16/20	32.8 ± 0.72	3.15 ± 0.46	17/20	42.3 ± 0.73	3.29 ± 0.67

Additionally, FLS is not utilized in approaches (a) and (c). Our approach (d) activates all modules. To validate the system's effectiveness and robustness, we conducted 20 experiments for each fabric placement configuration. Before each experiment, the initial fabric configurations and the platform plate were slightly repositioned. Fig. 14 present the fabric alignment results. The first row shows the initial alignment results from a third-person perspective. The last three rows depict the visual-servoing-based alignment results, captured from two D405 cameras and a handheld camera. The red arrow indicates the G-fabric's movement direction output using our approach. The results demonstrate that the proposed control framework effectively accomplishes fabric alignment. The fabric grasping remains stable without any dropping during movement, and the placement yields satisfactory results. This highlights the beneficial role of admittance control in fabric grasping and placement. The results also confirm the accuracy of the fabric frame Equation (4). Even under slope conditions, the G-fabric remains parallel to the A-fabric while maintaining a certain distance. This demonstrates the effectiveness of the proposed fabric definition. After the initial alignment, the system achieves near-predetermined alignment criteria, with minimal deviations when moving above the A-fabric. A relatively accurate initial alignment facilitates subsequent visual-servoing-based alignment, accelerating the overall alignment process. After visual-servoing adjustments, the fabrics are well aligned. Finally, by reactivating admittance control, the G-fabric is stably placed above the A-fabric. Adjusting the threshold value δ_3 allows fine-tuning of alignment accuracy.

Table II compares three metrics: success rate, running time, and alignment error, across four placement positions and the four approaches. Meanwhile, the visual comparison of success rates and alignment errors is presented in Fig. 15. From the success rate, it is evident that method (a) and method (b), lacking admittance control, achieve success rates of around 50%. The primary reasons for failure are unsuccessful grasping and dropping during visual-servoing processes. This emphasizes the importance of admittance control in ensuring stable contact between the fabric and the fixture. Additionally, due to the increased complexity of configurations in Case 3 and Case 4, their success rates are lower compared to the first two cases. In terms of running time, method (a) is the fastest, while method (d) is the slowest. The times for method (b) and method(c) are similar. The faster running time of method (a) is due to the absence of FLS compensation and admittance control, while method (d) activates both modules. Due to the adoption of FLS compensation in method (b) and our method (d), they exhibit lower alignment errors and lower standard deviations compared to methods (a) and (c). Specifically, for method (b), its success rate is lower due to the absence of admittance control. However, with FLS, if successful, its alignment error tends to be small. Similarly, for method (c), its performance contrasts sharply with method (b). Method (c) does not utilize FLS but employs admittance control, resulting in a slightly higher overall success rate. However, in terms of alignment error, method (c) exhibits larger alignment errors and is less stable (with a relatively large standard deviation). From an overall perspective, our method (d), employing both FLS and admittance control, ensures stable grasping/placement while controlling alignment errors concurrently, with a high success rate and the smallest alignment error.

TABLE III
COMPARATIVE RESULTS OF MANIPULATION PERFORMANCE UNDER FOUR DIFFERENT TYPES OF FABRICS AND FOUR COMPARATIVE FABRIC CONFIGURATIONS ILLUSTRATED IN FIG. 16.

	Success Rate	Running time (s)	Alignment Error (mm)
(1)	17/20	42.3 ± 0.73	3.29 ± 0.67
(2)	14/20	39.8 ± 1.06	4.72 ± 0.89
(3)	16/20	43.6 ± 1.29	4.25 ± 0.76
(4)	17/20	41.7 ± 1.27	4.62 ± 0.92

G. *Different Shape-size Fabric Alignment*

This section verifies the framework's generalization, focusing on alignment performance with different fabric shapes and configurations. To achieve this, three additional fabric shapes were cut based on the original fabric, as shown in Fig. 16. These four fabrics are commonly used in the stacking processes of collars and cuffs in clothing production. Fabric (1) represents the original shape, while fabrics (2)–(4) are newly added. Validation is performed using approach (d). The final manipulation results are shown in Fig. 16. The left side of each subplot represents the initial state, while the right side shows the final aligned state. Table III provides a detailed performance comparison for four various fabrics. For fabric 1, we directly provide the corresponding results from Case 4 - method (d) in Table II. The results demonstrate that the proposed alignment framework performs effectively across the four fabric shapes. However, there is a slight decrease in performance when manipulating fabric (2). This is because the fabric has large cutouts at both sides, leaving insufficient surface area for the suction cup to make stable contact and achieve a secure grip.

These results confirm the effectiveness of the proposed coarse-to-fine fabric alignment framework and highlight the importance of admittance control in maintaining stable fabric contact. By incorporating dynamic, online adaptive compensation based on FLS to address system disturbances, alignment

This article has been accepted for publication in IEEE Transactions on Automation Science and Engineering. This is the author's version which has not been fully edited and content may change prior to final publication. Citation information: DOI 10.1109/TASE.2025.3585644

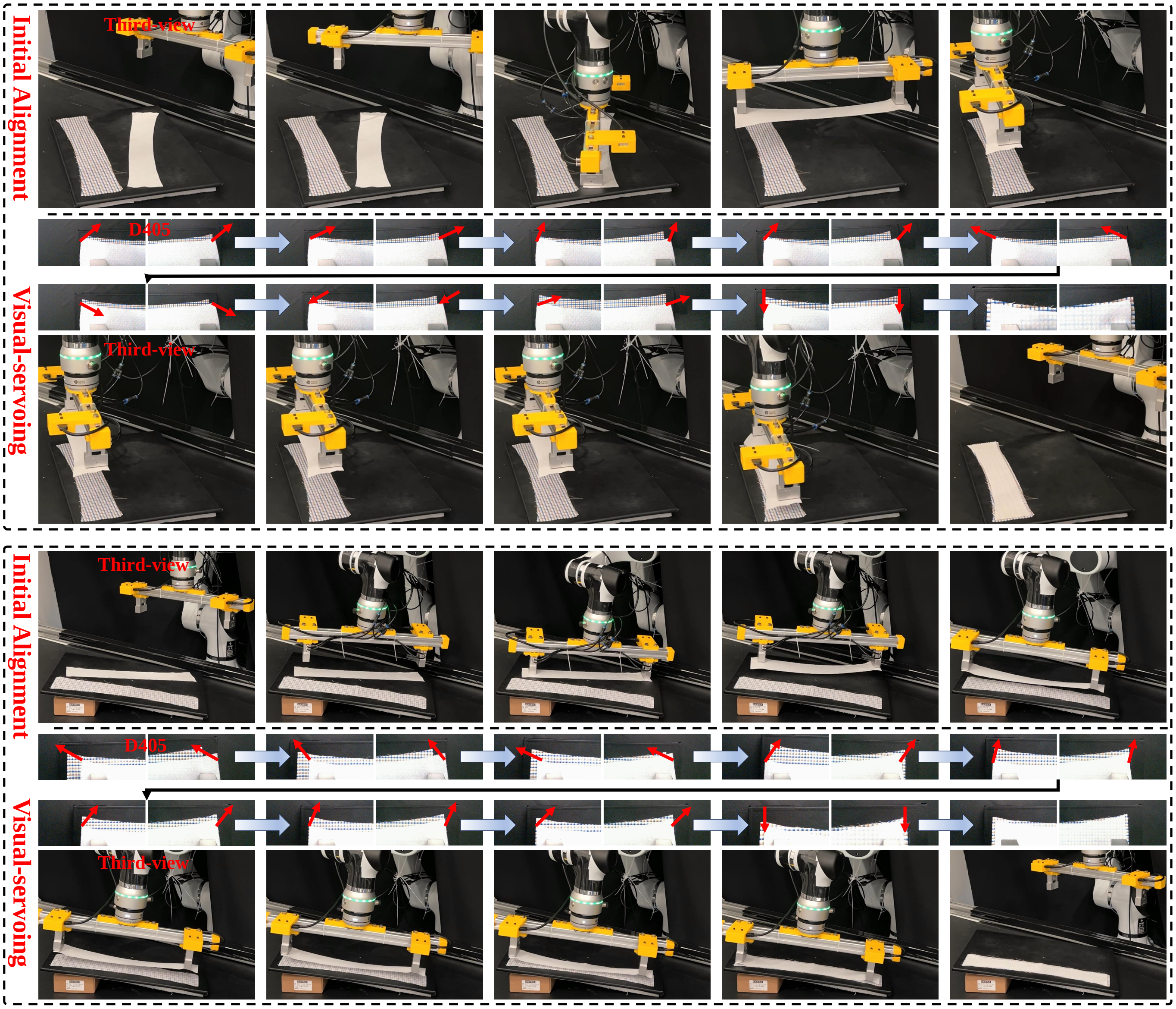

Fig. 14. Overall validations of the proposed fabric alignment framework, adopting the case shown in Fig. 7g (the first box) and Fig. 7i (the second box).

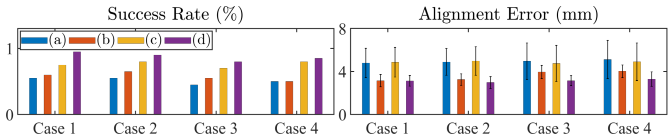

Fig. 15. The comparison of success rate and alignment error among four placement positions across four approaches.

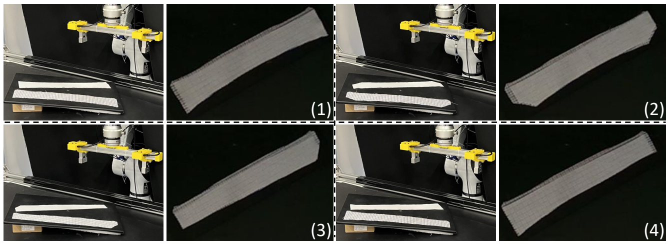

Fig. 16. Alignment results for four different fabric shapes and configurations.

accuracy is further improved. Additionally, the integration of visual servoing enables the proposed approach to adapt to the most commonly used fabric shapes. By designing specific fabric features, the system's generalization capability can be enhanced. Most fabric alignment devices rely on the pre-determined manner, which places significant demands on system model accuracy, increasing development complexity. In contrast, the proposed framework does not require a precise system model or symmetric grasping. As long as the fixture can securely grasp the fabric, the system can achieve alignment through visual servoing adjustments.

The proposed control method requires that the features on A-fabric remain visible during the visual servoing process. However, in practical applications, the program code imposes saturation limits on the actuator commands, temporary occlusions at certain time steps do not compromise the effectiveness of the servo alignment process, as long as the features reappear and are reacquired in subsequent time steps.

This article has been accepted for publication in IEEE Transactions on Automation Science and Engineering. This is the author's version which has not been fully edited and content may change prior to final publication. Citation information: DOI 10.1109/TASE.2025.3585644

VIII. CONCLUSIONS

The article presents a visual servoing-based fabric alignment framework for unstructured environments, addressing discretization, approximation, and saturation disturbances. Firstly, an optimization-based directed fabric frame is constructed to enable subsequent alignment servoing. Secondly, an SMC-based controller is proposed to integrate identification and control, while an FLS-based compensator is designed to handle system disturbances. Thirdly, admittance control is implemented to maintain stable contact between the gripper and the fabric. Finally, a Lyapunov stability proof is provided, demonstrating the boundedness of signals in the closed-loop system and the convergence of alignment errors. However, the framework has some limitations. For instance, the suction cup positions are fixed, making it difficult to adapt to various fabric types. Additionally, a calibrated depth camera is required, which may be challenging to implement in practical environments. Future work will focus on designing a fully model-free control scheme that does not rely on calibration or pre-measured fabric characteristics. Meanwhile, a sliding mechanism can be designed to adaptively adjust the distance between the two suction cups according to the fabric length.

REFERENCES

[1] B. Kehoe, S. Patil, P. Abbeel, and K. Goldberg, "A survey of research on cloud robotics and automation," *IEEE Transactions on automation science and engineering*, vol. 12, no. 2, pp. 398–409, 2015.

[2] M. Yu, K. Lv, C. Wang, Y. Jiang, M. Tomizuka, and X. Li, "Generalizable whole-body global manipulation of deformable linear objects by dual-arm robot in 3-d constrained environments," *The International Journal of Robotics Research*, p. 02783649241276886, 2023.

[3] J. Parker, R. Dubey, F. Paul, and R. Becker, "Robotic fabric handling for automating garment manufacturing," 1983.

[4] H. A. Kadi and K. Terzić, "Data-driven robotic manipulation of cloth-like deformable objects: The present, challenges and future prospects," *Sensors*, vol. 23, no. 5, p. 2389, 2023.

[5] J. Qi, G. Ma, J. Zhu, P. Zhou, Y. Lyu, H. Zhang, and D. Navarro-Alarcon, "Contour moments based manipulation of composite rigid-deformable objects with finite time model estimation and shape/position control," *IEEE/ASME Transactions on Mechatronics*, 2021.

[6] P. Zhou, P. Zheng, J. Qi, C. Li, H.-Y. Lee, Y. Pan, C. Yang, D. Navarro-Alarcon, and J. Pan, "Bimanual deformable bag manipulation using a structure-of-interest based neural dynamics model," *IEEE/ASME Transactions on Mechatronics*, 2024.

[7] M. Yu, K. Lv, H. Zhong, S. Song, and X. Li, "Global model learning for large deformation control of elastic deformable linear objects: An efficient and adaptive approach," *IEEE Transactions on Robotics*, vol. 39, no. 1, pp. 417–436, 2022.

[8] Z. Hu, T. Han, P. Sun, J. Pan, and D. Manocha, "3-d deformable object manipulation using deep neural networks," *IEEE Robotics and Automation Letters*, vol. 4, no. 4, pp. 4255–4261, 2019.

[9] S. Donaire, J. Borras, G. Alenya, and C. Torras, "A versatile gripper for cloth manipulation," *IEEE Robotics and Automation Letters*, vol. 5, no. 4, pp. 6520–6527, 2020.

[10] D. Hinwood, D. Herath, and R. Goecke, "Towards the design of a human-inspired gripper for textile manipulation," in *2020 IEEE 16th International Conference on Automation Science and Engineering (CASE)*. IEEE, 2020, pp. 913–920.

[11] T. Kim and Y.-L. Park, "Robotic platform for automatic alignment and placement of fabric patterns for smart manufacturing in garment industry," *International Journal of Precision Engineering and Manufacturing*, vol. 24, no. 9, pp. 1549–1561, 2023.

[12] D. Kragic, H. I. Christensen, *et al.*, "Survey on visual servoing for manipulation," *Computational Vision and Active Perception Laboratory, Fiskartorpsv*, vol. 15, p. 2002, 2002.

[13] D. Navarro-Alarcon, Y.-H. Liu, J. G. Romero, and P. Li, "Model-free visually servoed deformation control of elastic objects by robot manipulators," *IEEE Transactions on Robotics*, vol. 29, no. 6, pp. 1457–1468, 2013.

[14] D. Navarro-Alarcon, Y.-h. Liu, J. G. Romero, and P. Li, "On the visual deformation servoing of compliant objects: Uncalibrated control methods and experiments," *The International Journal of Robotics Research*, vol. 33, no. 11, pp. 1462–1480, 2014.

[15] D. Andronas, E. Kampourakis, K. Bakopoulou, C. Gkournelos, P. Angelakis, and S. Makris, "Model-based robot control for human-robot flexible material co-manipulation," in *2021 26th IEEE International Conference on Emerging Technologies and Factory Automation (ETFA)*. IEEE, 2021, pp. 1–8.

[16] G. Nicola, S. Mutti, E. Villagrossi, and N. Pedrocchi, "Depth image-based deformation estimation of deformable objects for collaborative mobile transportation," in *2023 32nd IEEE International Conference on Robot and Human Interactive Communication (RO-MAN)*. IEEE, 2023, pp. 2658–2664.

[17] S. D'Avella, A. M. Sundaram, W. Friedl, P. Tripicchio, and M. A. Roa, "Multimodal grasp planner for hybrid grippers in cluttered scenes," *IEEE Robotics and Automation Letters*, vol. 8, no. 4, pp. 2030–2037, 2023.

[18] K. P. Tee, R. Yan, and H. Li, "Adaptive admittance control of a robot manipulator under task space constraint," in *2010 IEEE International Conference on Robotics and Automation*. IEEE, 2010, pp. 5181–5186.

[19] Z. Li, B. Huang, Z. Ye, M. Deng, and C. Yang, "Physical human–robot interaction of a robotic exoskeleton by admittance control," *IEEE Transactions on Industrial Electronics*, vol. 65, no. 12, pp. 9614–9624, 2018.

[20] W. He, C. Xue, X. Yu, Z. Li, and C. Yang, "Admittance-based controller design for physical human–robot interaction in the constrained task space," *IEEE Transactions on Automation Science and Engineering*, vol. 17, no. 4, pp. 1937–1949, 2020.

[21] A. Seino, F. Tokuda, A. Kobayashi, and K. Kosuge, "Passive actuator-less gripper for pick-and-place of a piece of fabric," *Authorea Preprints*, 2024.

[22] A. Q. Keemink, H. Van der Kooij, and A. H. Stienen, "Admittance control for physical human–robot interaction," *The International Journal of Robotics Research*, vol. 37, no. 11, pp. 1421–1444, 2018.

[23] J. H. Cartwright and O. Piro, "The dynamics of runge–kutta methods," *International Journal of Bifurcation and Chaos*, vol. 2, no. 03, pp. 427–449, 1992.

[24] J. A. Andersson, J. Gillis, G. Horn, J. B. Rawlings, and M. Diehl, "Casadi: a software framework for nonlinear optimization and optimal control," *Mathematical Programming Computation*, vol. 11, pp. 1–36, 2019.

[25] H. Abdi and L. J. Williams, "Principal component analysis," *Wiley interdisciplinary reviews: computational statistics*, vol. 2, no. 4, pp. 433–459, 2010.

[26] F. Tokuda, A. Seino, A. Kobayashi, and K. Kosuge, "Cnn-based visual servoing for pose control of soft fabric parts," *Authorea Preprints*, 2023.

[27] K. Krishna and M. N. Murty, "Genetic k-means algorithm," *IEEE Transactions on Systems, Man, and Cybernetics, Part B (Cybernetics)*, vol. 29, no. 3, pp. 433–439, 1999.

[28] J. Qi, W. Ma, D. Navarro-Alarcon, H. Gao, and G. Ma, "Adaptive shape servoing of elastic rods using parameterized regression features and auto-tuning motion controls," *arXiv preprint arXiv:2008.06896*, 2020.

[29] X. Shao, P. Pustina, M. Stölzle, G. Sun, A. De Luca, L. Wu, and C. Della Santina, "Model-based control for soft robots with system uncertainties and input saturation," *IEEE Transactions on Industrial Electronics*, 2023.

[30] C. Lv, H. Yu, J. Chen, N. Zhao, and J. Chi, "Trajectory tracking control for unmanned surface vessel with input saturation and disturbances via robust state error ida-pbc approach," *Journal of the Franklin institute*, vol. 359, no. 5, pp. 1899–1924, 2022.

[31] C. Wen, J. Zhou, Z. Liu, and H. Su, "Robust adaptive control of uncertain nonlinear systems in the presence of input saturation and external disturbance," *IEEE Transactions on Automatic Control*, vol. 56, no. 7, pp. 1672–1678, 2011.

[32] J. Ma, S. S. Ge, Z. Zheng, and D. Hu, "Adaptive nn control of a class of nonlinear systems with asymmetric saturation actuators," *IEEE transactions on neural networks and learning systems*, vol. 26, no. 7, pp. 1532–1538, 2014.

[33] Q. Zhou, L. Wang, C. Wu, H. Li, and H. Du, "Adaptive fuzzy control for nonstrict-feedback systems with input saturation and output constraint," *IEEE Transactions on Systems, Man, and Cybernetics: Systems*, vol. 47, no. 1, pp. 1–12, 2016.

[34] Lagneau, K. Romain, M. Alexandre, and Maud, "Automatic shape control of deformable wires based on model-free visual servoing," *IEEE Robotics and Automation Letters*, vol. 5, no. 4, pp. 5252–5259, 2020.

[35] P. A. Ioannou and J. Sun, *Robust adaptive control*. Courier Corporation, 2012.

[36] J. Qi, G. Ma, P. Zhou, H. Zhang, Y. Lyu, and D. Navarro-Alarcon, "Towards latent space based manipulation of elastic rods using autoencoder models and robust centerline extractions," *Advanced Robotics*, vol. 36, no. 3, pp. 101–115, 2022.

[37] F. Tokuda, R. Murakami, A. Seino, A. Kobayashi, M. Hayashibe, and K. Kosuge, "Fixture-free 2d sewing using a dual-arm manipulator system," *IEEE Transactions on Automation Science and Engineering*, 2024.

Jiaming Qi received the Ph.D. degree in Control Science and Engineering and the M.S. degree in Integrated Circuit Engineering from Harbin Institute of Technology, Harbin, China, in 2023 and 2018, respectively. In 2019, he was a visiting Ph.D. student at the Robotics and Machine Intelligence Laboratory, The Hong Kong Polytechnic University. In 2023, he served as a Postdoctoral Research Fellow in the Centre for Garment Production Limited, Department of Computer Science, University of Hong Kong, Hong Kong SAR, China. He is currently an Assistant Professor in the College of Mechanical and Electrical Engineering at Northeast Forestry University, Harbin, China. His research interests lie in the areas of deformable object manipulation, visual servoing, human-robot collaboration, and robot compliance control.

Liang Lu received M.Sc. degree in mechatronics from Hefei University of Technology in 2017 and Ph.D. degree in automation and robotics from the Center for Automation and Robotics, UPM-CSIC, in 2021. He was a postdoctoral fellow at the Italian Institute of Technology from Dec. 2021 to Mar. 2023. He is currently a postdoctoral fellow at TansGP and the University of Hong Kong. His research interest includes active perception, scene understanding and field robotics.

Lei Yang is a lecturer at the University of Hong Kong. He received his bachelor's degree and Ph.D. degree from Dalian University of Technology, in 2012 and 2018, respectively. His research interests include geometric modeling, computer vision, and robotics.

Yan Ding is a researcher at the Shanghai AI Laboratory. He earned his Ph.D. in Computer Science from the State University of New York at Binghamton in 2024. He holds a Master's degree in Computer Science and Technology from the College of Computer Science at Chongqing University (2019) and a Bachelor's degree in Mechatronic Engineering from the College of Mechanical Engineering at Chongqing University (2016). His research focuses on spatial intelligence for robotics, aiming to enable robots to understand and interact with the real world, and on skill learning for robotics, empowering robots to effectively transform the real world.

Pai Zheng (Senior Member, IEEE) received the dual bachelor's degrees in mechanical engineering (major) and computer science and engineering (minor) from the Huazhong University of Science and Technology, Wuhan, China, in 2010, the master's degree in mechanical engineering from Beihang University, Beijing, China, in 2013, and the Ph.D. degree in mechanical engineering from The University of Auckland, Auckland, New Zealand, in 2017. He has been a Research Fellow with the Delta-NTU Corporate Laboratory for Cyber-Physical Systems, School of Electrical and Electronic Engineering, Nanyang Technological University (NTU), Singapore, from January 2018 to September 2019. He is currently an Assistant Professor with the Department of Industrial and Systems Engineering, The Hong Kong Polytechnic University. His research interests include smart product-service systems, human–robot collaboration, and smart manufacturing systems. He is a member of HKIE, CMES, and ASME. He serves as an Associate Editor for Journal of Intelligent Manufacturing and Journal of Cleaner Production, an Editorial Board Member for the Journal of Manufacturing Systems and Advanced Engineering Informatics, and a guest editor/reviewer for several high impact international journals in the manufacturing and industrial engineering field.

David Navarro-Alarcon (Senior Member, IEEE) received the Ph.D. degree in mechanical and automation engineering from The Chinese University of Hong Kong (CUHK), in 2014. From 2014 to 2017, he worked as a Postdoctoral Fellow and then as a Research Assistant Professor at the T Stone Robotics Institute of CUHK. Since 2017, he has been with The Hong Kong Polytechnic University (PolyU), where he is currently an Associate Professor with the Department of Mechanical Engineering, and the Principal Investigator of the Robotics and Machine Intelligence Laboratory. His current research interests include perceptual robotics and control systems. Dr. Navarro-Alarcon currently serves as an Associate Editor of the IEEE TRANSACTIONS ON ROBOTICS.

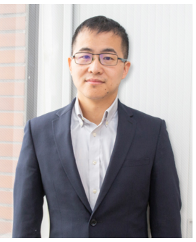

Jia Pan (Senior Member, IEEE) received the Ph.D. degree in computer science from the University of North Carolina at Chapel Hill, Chapel Hill, NC, USA, in 2013. He is currently an Associate Professor with the Department of Computer Science, University of Hong Kong, Hong Kong. He is also a member of the Centre for Garment Production Limited, Hong Kong. His research interests include robotics and artificial intelligence as applied to autonomous systems, particularly for navigation and manipulation in challenging tasks such as effective movement in dense human crowds and manipulating deformable objects for garment automation.

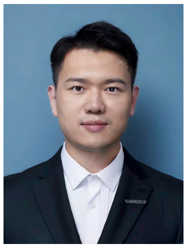

Peng Zhou received his Ph.D. degree in robotics from The Hong Kong Polytechnic University, Hong Kong SAR, in 2022. In 2021, he was a Visiting Researcher at the Robotics, Perception, and Learning Lab, KTH Royal Institute of Technology, Stockholm, Sweden. From 2022 to 2024, he was a Postdoctoral Research Fellow at the Department of Computer Science, The University of Hong Kong. He is currently an Assistant Professor at the School of Advanced Engineering, Great Bay University (GBU). His research interests include deformable object manipulation, robotic perception and learning, and task and motion planning.